PNAS RESEARCH ARTICLE | BIOCHEMISTRY

OptoRibo-seq for spatiotemporally resolved mapping of the local protein translatome

Ruixuan Wang[a,1], Ruixiang Wang[b,1], Wentao Wang[a], Yanjun Liu[a], Fu Zheng[a], Huixin Luo[a,2], Peng R. Chen[a,b,2], and Peng Zou[a,b,c,d,2]

Affiliations are included on p. 11.

Edited by Xin Zhang, Westlake University, Hangzhou, China; received July 22, 2025; accepted April 9, 2026 by Editorial Board Member Stephen J. Benkovic

Localized protein translation occurs in numerous subcellular compartments and regulates diverse biological processes by rapidly changing protein compositions in response to subcellular needs. Existing assays for subcellular local translation either require physical isolation, which is prone to contamination and loss of material, or imaging-based readout, which is often hampered with low throughput. In this study, we report the development of the optoRibo-seq method that features photoactivatable enzyme-mediated proximity labeling of ribosomes in genetically specified subcellular locations. We demonstrate the spatial specificity of optoRibo-seq at the endoplasmic reticulum (ER) membrane, with a temporal resolution of 1 min. In cells undergoing chemically induced ER stress, optoRibo-seq allowed mapping of the dynamic changes in the ER-proximal translatome, identifying transcripts involved in protein folding and targeting. Our strategy provides a general platform for spatiotemporally resolved profiling of subcellular protein translation.

proximity labeling | genetic codon expansion | ribosome profiling | biotin ligase | ER stress

Significance

Local protein synthesis is essential for the spatiotemporal regulation of gene expression across diverse biological processes. However, existing tools for studying localized translation often suffer from limited throughput and spatial resolution. In this study, we present optoRibo-seq, an optogenetic proximity ribosome profiling method enabled by a genetic code expansion-assisted bioorthogonal decaging strategy. We demonstrate that optoRibo-seq achieves high spatial specificity in capturing ribosome-associated transcripts at the endoplasmic reticulum under both physiological and stress conditions. This technique provides a versatile and precise platform for profiling subcellular translation with spatiotemporal control.

In eukaryotic cells, the subcellular localization of proteins is often essential to their biological functions. While posttranslational targeting directs many proteins to specific locations, protein localization can also occur through localized protein translation, which plays a key role in diverse biological activities, such as cell migration (1), differentiation (2), and synaptic plasticity (3). Local protein translation is especially prominent at the endoplasmic reticulum membrane (ERM) (4), where ribosome-mRNA complexes anchor to produce proteins destined for secretion or integration into the plasma membrane. In neuronal synapses, local protein synthesis bypasses RNA transcription, enabling rapid adjustments in protein composition to meet specific subcellular demands (5). Dysregulation of local translation has been linked to neurodegenerative diseases, including Alzheimer's disease (6) and amyotrophic lateral sclerosis (7).

Traditional methods for studying localized protein translation primarily rely on imaging techniques, such as SINAPs (8) and Puro-PLA (9). Although these fluorescence imaging-based methods offer high spatial resolution for mapping ribosome-bound mRNAs near subcellular landmarks, their throughput is often limited. The recent development of RIBOmap has improved multiplexity (10), but this approach requires sophisticated in situ sequencing setups. Additionally, all imaging-based techniques need prior knowledge of RNA sequences to design complementary oligos. Alternatively, ribosome-bound mRNAs can be mapped using cell-specific [e.g., TRAP (11)] or subcellular-specific ribosome isolation [e.g., microdissection (12)] combined with sequencing, such as ribosome profiling (13). However, these physical isolation techniques can introduce contamination, lose material, and are not generally applicable for mapping the translatome of any specified subcellular compartments of interest (14).

Proximity labeling provides a powerful method to examine the molecular composition of distinct subcellular regions with high spatial precision (15). For instance, proximity-specific ribosome profiling uses a subcellularly localized bacterial biotin ligase, BirA, to label nearby acceptor peptide (AP)-tagged ribosomes. However, achieving high spatial resolution for subcellular translatome mapping requires precise temporal control over biotinylation to limit ribosome diffusion. In prior proximity-specific ribosome profiling studies (16, 17), biotinylation was triggered by adding biotin to cells preconditioned in biotin-deprived culture media. Since biotin is vital for mammalian cells, biotin starvation may induce cellular stress, complicating data analysis. Recently, Weissman and coworkers developed LOCL-TL, which used the light-sensitive LOV domain to gate BirA activity. LOCL-TL identified the local translatome of the mammalian outer mitochondrial membrane (OMM) region (18).

In this study, we report the development of a photoactivatable proximity ribosome profiling technique (optoRibo-seq) using a photodecaging strategy. In our method,

Author contributions: Ruixuan Wang, P.R.C., and P.Z. designed research; Ruixuan Wang, Ruixiang Wang, W.W., Y.L., F.Z., and H.L. performed research; Ruixuan Wang and Ruixiang Wang contributed new reagents/analytic tools; Ruixuan Wang, Ruixiang Wang, and P.Z. analyzed data; and Ruixuan Wang, Ruixiang Wang and P.Z. wrote the paper.

The authors declare no competing interest.

This article is a PNAS Direct Submission. X.Z. is a guest editor invited by the Editorial Board.

[1]Ruixuan Wang and Ruixiang Wang contributed equally to this work.

[2]To whom correspondence may be addressed. Email: luohuixin@imm.ac.cn, pengchen@pku.edu.cn, or zoupeng@pku.edu.cn.

This article contains supporting information online at https://www.pnas.org/lookup/suppl/doi:10.1073/pnas.2519235123/-/DCSupplemental.

Published May 20, 2026.

enzyme-mediated proximity biotinylation was initially blocked by substituting the essential catalytic residue in *Escherichia coli* biotin ligase (BirA) with a photocaged amino acid, N^{ε}-[(1-(6-Nitrobenzo[d][1,3]dioxol-5yl)ethoxy)carbonyl]-*L*-lysine (ONPK). Upon 365 nm UV irradiation, the *o*-nitrobenzyl caging group was removed, initiating ribosome biotinylation within 1 min (Fig. 1*A*). Following monosome isolation and affinity purification, RNA footprints were extracted for high-throughput sequencing analysis (Fig. 1*A*). We applied optoRibo-seq to the ERM in human embryonic kidney 293 T (HEK293T) cells,

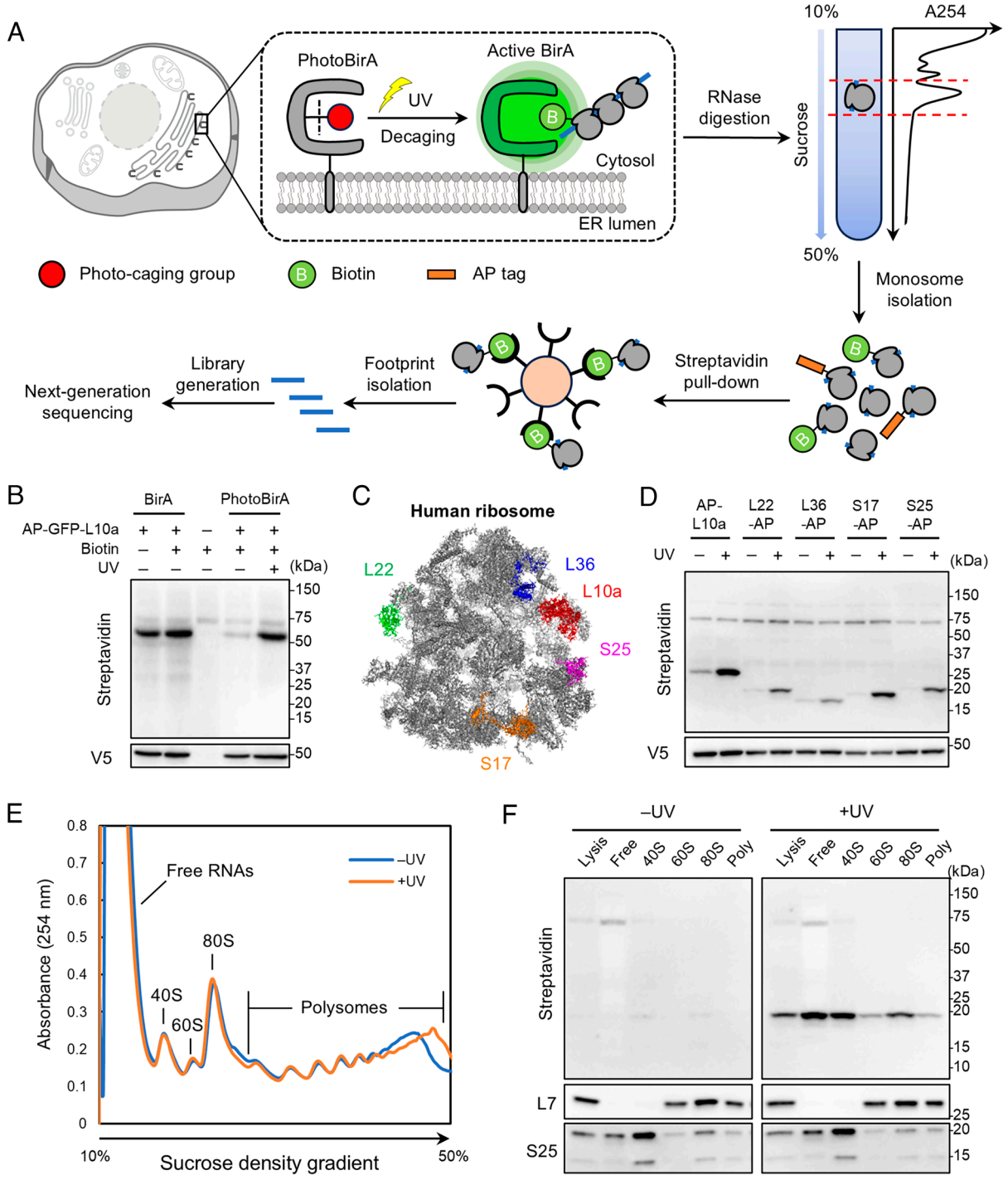

Fig. 1. OptoRibo-seq with the engineered photoactivatable biotin ligase photoBirA. (*A*) Schematic representation of optoRibo-seq for profiling the ER-proximal translatome. PhotoBirA is engineered through GCE, incorporating a photocaged lysine analog (ONPK) that replaces the catalytic lysine residue (Lys183) of BirA. Targeting the ERM is achieved by fusing photoBirA with the translocon Sec61β. Upon exposure to 365 nm UV, photoBirA is rapidly activated to catalyze the biotinylation of proximal AP-tagged ribosomes. Following ultracentrifugation and affinity purification to isolate biotinylated monosomes, RNA footprints are extracted for next-generation sequencing analysis. (*B*) Streptavidin blot analysis of the ribosomal protein L10a (AP-GFP-L10a) biotinylated by photoBirA. HEK293T cells expressing either wild-type BirA or photoBirA were incubated with 50 μM biotin and UV-irradiated for 10 min. (*C*) Structural representation of five candidate ribosomal proteins on the ribosome, including L10a (red), L22 (green), L36 (blue), S17 (orange), and S25 (magenta). (PDB: 4V6X). (*D*) Streptavidin blot analysis demonstrating the biotinylation efficiency of five AP-tagged ribosomal proteins using photoBirA-Sec61β. (*E*) UV profile of cell lysate fractionated by sucrose density gradient centrifugation, with absorbance measured at 254 nm. Peaks of free RNAs, ribosomal subunits (40S and 60S), monosomes (80S), and polysomes are indicated. (*F*) Western blot analysis of ribosomal fractions before and after photoBirA labeling. Streptavidin blot indicates biotinylation signals. "Lysis": whole cell lysate; "Free": free RNA fractions; "40S": small subunits; "60S": large subunits; "80S": monosomes; "Poly": polysomes.

identifying 299 locally translated mRNAs with over 90% specificity. Using optoRibo-seq to map dynamic changes in the ER-proximal translatome under ER stress, we elucidated the role of ER-proximal translation in the unfolded protein response (UPR), including the translation of proteins involved in protein folding and targeting.

Results

Design and Development of OptoRibo-seq. We began by temporally controlling BirA's catalytic activity using a photodecaging strategy. BirA conjugates *D*-biotin to the lysine residue of an engineered 15-amino acid AP tag via two steps (19): i) BirA catalyzes the reaction between *D*-biotin and ATP, generating the reactive intermediate biotinyl-5'-AMP, and ii) BirA facilitates the formation of an amide bond between biotinyl-5'-AMP and the Lys10 residue in the AP tag (19). In typical mammalian cell culture, *D*-biotin (vitamin H) is routinely supplemented, and due to BirA's high catalytic efficiency, it can use endogenous *D*-biotin levels to label AP-tagged protein targets. For instance, when BirA and AP-tagged ribosomal protein L10a (AP-GFP-L10a) were coexpressed in the cytoplasm of HEK293T cells, biotinylation occurred spontaneously without the need for exogenous *D*-biotin (Fig. 1*B*).

In our prior work, we engineered a photocontrollable biotin ligase termed photoTurbo to map subcellular proteomes (20, 21). Building on this approach, we substituted the critical Lys183 residue in BirA's catalytic domain (19) with the photocaged lysine analog ONPK using genetic codon expansion (GCE) to control BirA's activity (*SI Appendix*, Fig. S1*A*), creating photoBirA. In HEK293T cells coexpressing AP-GFP-L10a, photoBirA was almost entirely inactive, even with 50 μM *D*-biotin in the culture medium (Fig. 1*B*). However, after 10 min of 365 nm UV irradiation, the *o*-nitrobenzyl caging group was selectively removed, producing a strong biotinylation signal comparable to wild-type BirA (Fig. 1*B*). We also tested another unnatural amino acid, *o*-nitrobenzyl-*L*-lysine (ONBK), but its lower expression in HEK293T cells led to reduced activity, likely due to differences in recognition by aminoacyl tRNA synthetase (*SI Appendix*, Fig. S1 *B* and *C*). We thus chose ONPK for all subsequent experiments.

Next, we screened five ribosomal proteins for AP tagging. Ribosomal proteins L10a (16) and L22 (22) have been previously used for epitope tagging, and we additionally selected L36, S17, and S25, whose C termini were solvent-exposed on the ribosome surface (Fig. 1*C*). The AP tag was fused to the N terminus of L10a and the C termini of the other four proteins. Biotinylation was assessed by immunofluorescence imaging and western blotting of HEK293T cells coexpressing photoBirA and AP-tagged ribosomal proteins, with and without UV irradiation. Among these candidates, AP-L10a, S17-AP, and S25-AP showed higher biotinylation signals (Fig. 1*D*). While AP-L10a and S17-AP produced biotinylation signals in the nucleus, S25-AP biotinylation was restricted to the cytoplasm (*SI Appendix*, Fig. S2*A*). We therefore chose S25-AP as the affinity handle for ribosome enrichment in further experiments.

We generated a HEK293T cell line stably expressing S25-AP (*SI Appendix*, Fig. S2*B*). Ribosome profiling analysis at the whole-cell level confirmed that S25-AP expression did not interfere with global translation (*Pearson's r* = 0.90, *SI Appendix*, Fig. S2*C* and Dataset S1). We then applied sucrose density gradient centrifugation to isolate ribosome fractions (Fig. 1*E*). The 40S (small subunit), 60S (large subunit), 80S (monosomes), and polysome fractions were collected to assess S25-AP assembly efficiency. Western blot analysis confirmed that S25-AP was correctly incorporated into ribosomal small subunits and intact ribosomes, with over half of the 80S ribosomes containing biotinylated S25-AP (Fig. 1*F*). Together, these results demonstrate the feasibility of optoRibo-seq, identifying S25-AP as the optimal substrate with high labeling and ribosome incorporation efficiency.

ER-Proximal Translatome Profiling by OptoRibo-seq. We applied optoRibo-seq to profile local protein translation at the ERM, a key site for cotranslational targeting of secretory pathway proteins, including ER-resident, secreted, and plasma membrane proteins (23). During translation, the binding of nascent signal sequences to signal recognition particles (SRPs) directs translating ribosomes to translocons on the ERM surface. This peptide-based localization mechanism helps ensure precise subcellular targeting of newly synthesized secretory pathway proteins. To label ER-proximal AP-tagged ribosomes, we fused photoBirA with the ER translocon subunit Sec61β.

The spatial specificity of optoRibo-seq is directly tied to the temporal precision of photodecaging. Given the dynamic nature of ribosomes, which continuously recycle between assembled and disassembled states, biotinylated AP-tagged ribosomes can potentially diffuse into other subcellular regions, degrading spatial resolution over time. To enhance both spatial and temporal control, we aimed to minimize the labeling duration. We tested photoBirA labeling times of 2, 5, and 10 min, quantifying S25-AP biotinylation by anti-AP tag and streptavidin blotting (*SI Appendix*, Fig. S3*A*). Nearly 90% of AP-tagged ribosomes were biotinylated within 5 min, highlighting the efficiency of photoBirA (*SI Appendix*, Fig. S3*B*). Encouragingly, even with only 1 min of UV decaging, approximately 30% of ribosomes were labeled (Fig. 2*A* and *SI Appendix*, Fig. S3*C*). Fluorescence microscopy showed strong colocalization of biotinylation with ERM-targeted photoBirA after decaging (Fig. 2*B*). Moreover, the 1-min UV irradiation protocol did not significantly affect cell viability or protein translation (*SI Appendix*, Fig. S3 *D* and *E* and Dataset S1). Taken together, these findings demonstrate the potential of optoRibo-seq to achieve temporal resolution as high as 1 min for profiling local translatomes.

To further enhance spatial specificity, we created a HEK293T cell line stably expressing untargeted photoBirA in the cytosol (photoBirA-NES), allowing labeling of AP-tagged ribosomes distant from the ERM. Ratiometric analysis of optoRibo-seq data from ERM- *versus* cytosol-localized photoBirA enabled us to assess the "proximity" of ribosome-bound transcripts to these landmarks, akin to drawing a "contour map" of localized transcripts (27). Triplicate biological replicates for each sample yielded highly consistent enrichment levels, with Pearson's correlation coefficients above 0.90 among replicates (*SI Appendix*, Fig. S4*A*). After affinity purification of biotinylated ribosomes, RNA footprint extraction, and cDNA library construction, we obtained "Enrich" (after affinity purification) and "Input" (preaffinity purification) samples of ERM and cytosolic optoRibo-seq datasets (Fig. 2*C*, *SI Appendix*, Fig. S4 *B* and *C*, and Dataset S2). Cycloheximide was included throughout to arrest translation and preserve ribosome–mRNA complexes.

We compared transcripts enriched in the ERM optoRibo-seq dataset to the input ("ERM Enrich versus Input") or those enriched in the cytosolic optoRibo-seq dataset ("ERM versus Cytosol Enrich"). DEseq2 analysis identified 2,175 and 1,002 enriched transcripts in the above two datasets, respectively ($\log_2$FoldChange ≥ 0.3 and adjusted *P*-value < 0.05, Fig. 2*D*). The majority of reads were 20 to 40 nucleotides in length with partial 3-nt periodicity, consistent with conventional Ribo-seq profiles produced by micrococcal nuclease (MNase) digestion (*SI Appendix*, Fig. S4 *D* and *E*).

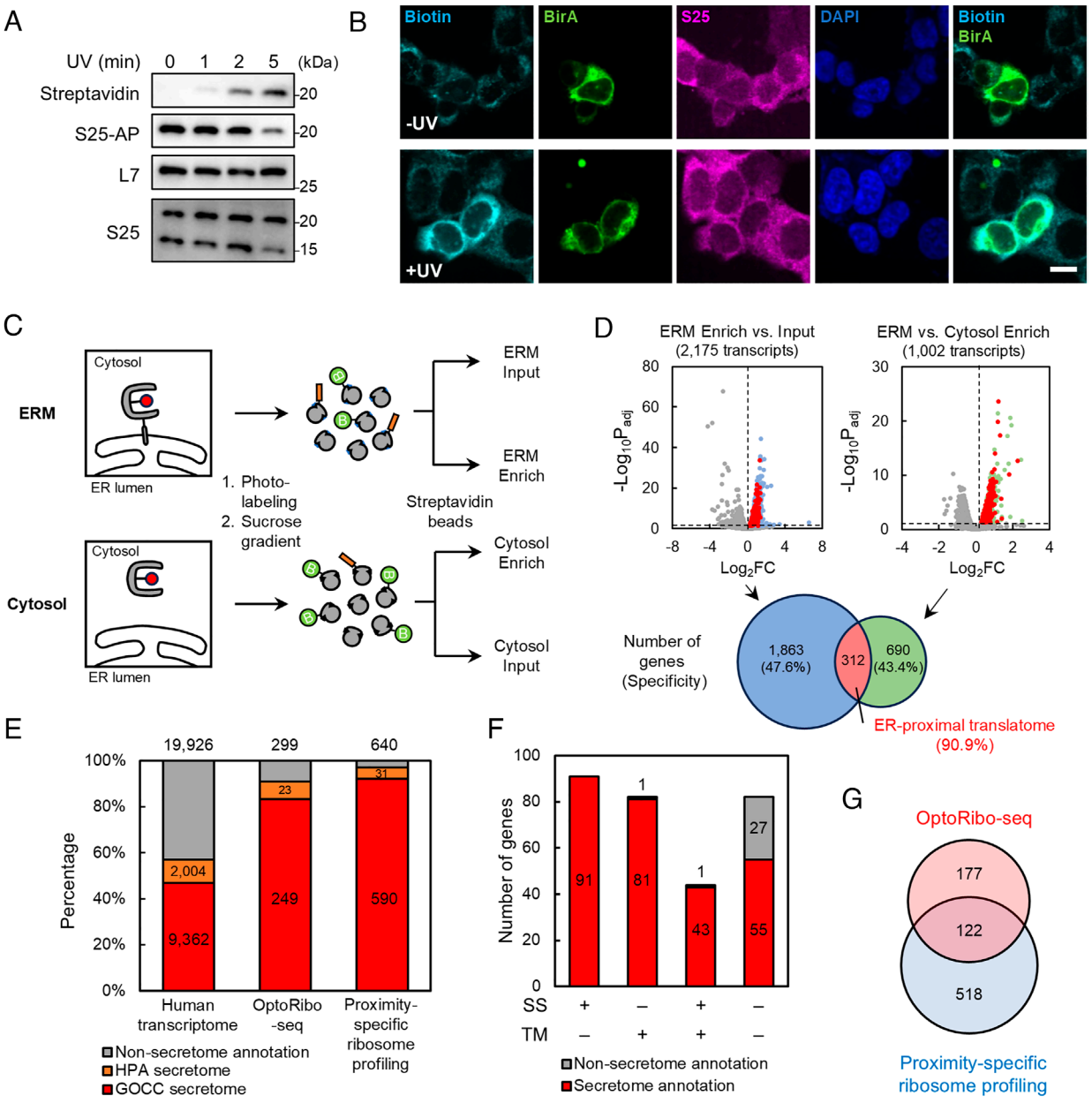

Fig. 2. Profiling the ER-proximal translatome with ER membrane-targeted optoRibo-seq. (*A*) Western blot analysis of S25-AP biotinylation in monosomes following decaging for 1, 2, or 5 min. (*B*) Immunofluorescence images showing biotinylation of S25-AP by photoBirA-Sec61β after 1 min decaging. Biotin (cyan) indicates the proximity labeling signal. PhotoBirA-Sec61β and S25-AP are visualized in green and magenta, respectively. Nuclei are stained with DAPI (blue). (Scale bar: 10 μm.) (*C*) Sample preparation workflow for optoRibo-seq in profiling the ER-proximal translatome. "ERM Input" and "Cytosol Enrich" samples serve as negative controls for optoRibo-seq data analysis. (*D*) Volcano plots showing DESeq2 analysis of the ERM optoRibo-seq dataset, comparing RNAs enriched by ERM-targeted photoBirA against either the input (*Left*) or RNAs enriched by cytosolic photoBirA (*Right*). The horizontal dashed line indicates an adjusted p-value of 0.05, while the vertical dashed line represents the cutoff for $\log_2$FoldChange (FC) of 0.3. Adjusted p-value was calculated using the Wald test in DESeq2 software. ER-proximal translatome is defined as the overlap of the two enrichment datasets (red region in the Venn diagram and red dots in the volcano plots). (*E*) Comparison of secretome specificity between optoRibo-seq and proximity-specific ribosome profiling (16). The number of transcripts in each condition is indicated in the columns. Secretome annotation was generated from the Gene Ontology Cellular Component (GOCC) (24), the Human Protein Atlas (HPA) (25), and the MitoCarta 3.0 (26) databases. (*F*) Analysis of signal sequence (SS) or transmembrane domain (TM) annotations in transcripts identified in our ER-proximal translatome dataset. (*G*) Venn diagram comparing the datasets of ERM optoRibo-seq and proximity-specific ribosome profiling (16).

The high P-site occupancy within coding sequences (CDS) further confirms the quality of the enriched ribosome footprints (*SI Appendix*, Fig. S4*F*). The overlap of these two datasets contained 312 RNAs, including 299 mRNAs, which we defined as our ER-proximal translatome. Of these, 272 mRNAs (91.0%) encode proteins previously annotated in the secretome according to Gene Ontology (24) or Human Protein Atlas (25) (Fig. 2*E*). This high spatial specificity is comparable to previously reported proximity ribosome profiling results (16). To visualize the relative enrichment of these transcripts in the ERM-targeted and cytosolic optoRibo-seq datasets, we plotted the enrichment ratios (ERM Enrich/Input versus Cytosol Enrich/Input; *SI Appendix*, Fig. S4*G*). While 56 transcripts exhibit enrichment in both datasets, a subset of 31 RNAs displays strong ERM enrichment with minimal cytosolic enrichment, consistent with preferential ER-proximal translation.

Of the 299 mRNAs analyzed, the majority encoded proteins containing either signal sequences (173/299) or transmembrane domains (126/299), features that are consistent with the characteristics of secretome-associated proteins (Fig. 2*F*). Gene Ontology Cellular Component (GOCC) analysis of the ER-proximal

translatome showed an overrepresentation of terms related to the secretory pathway, such as "ER lumen", "extracellular matrix", and "basement membrane" (*SI Appendix*, Fig. S4*H*). Notably, our ER-proximal translatome only partially overlapped (122 out of 299) with a previously reported proximity-specific ribosome profiling dataset of 640 transcripts (Fig. 2*G*) (16), likely due to differences in activation methods (decaging *versus* biotin starvation) and the specific ribosomal protein used for AP-tagging (S25 versus L10a).

Verification of ER-Proximal Translatome. To validate the accuracy of our dataset, we used single-molecule fluorescence in situ hybridization (smFISH) to visualize mRNA molecules in formaldehyde-fixed cells directly. Given that the ER network occupies a large portion of cellular space, assessing ER-proximity solely by localization proved challenging. We thus adopted a digitonin extraction strategy, which selectively retained ER-bound mRNA molecules while releasing free cytosolic RNAs (Fig. 3*A*). This approach has been previously applied to isolate and identify ER-bound mRNAs in HEK293, HeLa, and COS-7 cells (28, 29). Western blotting confirmed that digitonin extraction efficiently isolated ERM components and ERM-bound ribosomes (*SI Appendix*, Fig. S5). When digitonin extraction was performed after pretreating cells with the translation inhibitor puromycin, which disassembled ribosomes, a marked reduction in ERM-bound ribosomes was observed, demonstrating that translation-dependent mRNA-ERM association was disrupted by puromycin, thus allowing mRNA release during digitonin extraction (Fig. 3*A*).

Using this approach, we performed 3D-stack smFISH imaging in HEK293T and HeLa cells to examine the localization of target mRNAs with and without puromycin treatment and digitonin extraction. We quantified the number of mRNA FISH foci across z-axis sections (Fig. 3 *A* and *B*). For the mRNA of calnexin (*CANX*), which was identified in both our ER-proximal translatome and previous studies, the FISH signal decreased only slightly following digitonin extraction alone (2.2% reduction, $P = 0.75$ for HeLa; 7.4% reduction, $P = 0.19$ for HEK293T). However, in the presence of both puromycin and digitonin (Puro + Dig), the signal dropped significantly (47.6% reduction, $P = 3.35 \times 10^{-10}$ for HeLa; 39.6% reduction, $P = 3.35 \times 10^{-18}$ for HEK293T), indicating strong ERM localization of *CANX* mRNAs, with most of them dependent on ribosomal binding to the ERM (Fig. 3*B*, *SI Appendix*, Fig. S5 *B* and *C*, and Dataset S3). In contrast, the cytosolic mRNA *ACTB* showed a significant decrease after digitonin extraction alone (53.4% reduction, $P = 2.42 \times 10^{-14}$ for HeLa), independent of puromycin treatment (Fig. 3*B* and Dataset S3).

We further examined three transcripts uniquely identified in our dataset, namely *COPB2*, *HSP90AB1*, and *SERPINB6*, which lacked prior secretome annotations and were missing in proximity-specific ribosome profiling (16). *COPB2* encodes a coatomer subunit involved in Golgi-to-ER transport (30), *HSP90AB1* encodes the molecular chaperone heat shock protein 90-beta (31), and *SERPINB6* encodes serpin B6, which regulates serine proteases (32). Each of these mRNAs showed a pattern similar to the positive control, *CANX*, with the most significant reduction in mRNA signal occurring when both puromycin treatment and digitonin extraction were applied (Fig. 3*B* and Dataset S3). These findings validate the accuracy of our ER-proximal translatome dataset and confirm that ERM-targeting of these mRNAs depends on active ribosomal translation. Both sequence prediction and RiboWaltz analysis of our optoRibo-seq data demonstrated that these three transcripts lacked a signal sequence structure, distinguishing them markedly from the known signal sequence-containing transcript *CANX* (Fig. 2*F* and *SI Appendix*, Fig. S5*D*) (33). These observations suggest that ER association of these transcripts depends on ongoing translation but is not readily explained by canonical signal peptide-mediated targeting. The molecular mechanism underlying their ER-proximal translation remains to be determined.

In an effort to extend the application of optoRibo-seq to other subcellular locations, we sought to map the local translatome at the outer mitochondrial membrane (OMM). To enable OMM-targeted optoRibo-seq, we fused photoBirA to the transmembrane domain of MAVS, an established OMM-targeting sequence, and applied a ratiometric analysis workflow analogous to that used in our ER-targeted experiments (*SI Appendix*, Fig. S6*A*). This analysis identified 1,586 and 1,587 transcripts significantly enriched relative to input and cytosol controls, respectively ($\log_2$FoldChange ≥ 0.3, adjusted P-value < 0.05). The intersection of these two datasets yielded 1,061 transcripts (containing 1,036 mRNAs), which we defined as the OMM-proximal translatome (*SI Appendix*, Fig. S6*B* and Dataset S4). Among these, 58 transcripts (5.6%) encoded mitochondrial proteins, as annotated by MitoCarta 3.0 (26), a proportion comparable to that observed with previous proximity RNA labeling approaches such as APEX-seq (34), but lower than reported by CAP-seq (35) or LOCL-TL (18) (*SI Appendix*, Fig. S6*C*). The overlap between OMM-proximal translatome datasets obtained by optoRibo-seq and LOCL-TL (18) yielded only 18 RNAs (*SI Appendix*, Fig. S6*D*). Together, these results suggested that optoRibo-seq faces limitations for studying local translation at the OMM and requires further optimizations.

Dynamic Mapping of ER-Proximal Translatome under Stress. Translation is tightly regulated in response to various stimuli, including cellular stress. A major form of such stress is ER stress, which arises when misfolded or unfolded proteins accumulate in the ER lumen. This accumulation activates the UPR pathway, a signaling network that aims to restore ER homeostasis or, if unresolved, initiates apoptosis (36). One key branch of the UPR involves PERK-mediated phosphorylation of the translation initiation factor eIF2α, which inhibits the formation of the eIF2-GTP-Met-$tRNA_i$ ternary complex (37). This leads to a global reduction in translation while selectively enhancing the translation of stress-responsive transcription factors.

Leveraging the high temporal precision (1-min resolution) of photoBirA-mediated labeling, we investigated the dynamics of ER-proximal translation during acute stress. To induce ER stress, HEK293T cells were treated with thapsigargin (Tg), a SERCA inhibitor that disrupts ER calcium homeostasis. Successful induction was confirmed by time-dependent upregulation of the ER stress marker BiP (*SI Appendix*, Fig. S7*A*). Using the optoRibo-seq workflow, we profiled the ER-proximal translatome at 0, 0.5, 2, and 8 h post-Tg treatment and identified 180 (0 h), 396 (0.5 h), 308 (2 h), and 336 (8 h) transcripts enriched at the ER membrane respectively (*SI Appendix*, Fig. S7 *B*–*E* and Dataset S5). The union of these datasets yielded 872 transcripts. To remove lowly expressing transcripts, we excluded genes with zero FPKM (fragments per kilobase per million mapped fragments) values at any time point or having a total FPKM below 10 across all four time points. This filtering resulted in 331 transcripts for further analysis. Gene Ontology analysis of these 331 transcripts revealed enrichment in UPR-related pathways, including protein targeting, folding, and ER stress response (*SI Appendix*, Fig. S8*A*).

Heatmaps and dendrograms of our dataset containing 331 transcripts uncovered five transcript clusters with distinct temporal profiles (Fig. 4*A*). Clusters 1-3, comprising over half the dataset, showed diverse patterns of translational down-regulation (Fig. 4*B*). In contrast, Clusters 4 and 5 (48.6%, 162 transcripts) were enriched for canonical UPR genes such as *HSPA5* (BiP), *OS9* and *PDIA3*. Cluster 4 transcripts remained largely unchanged at early

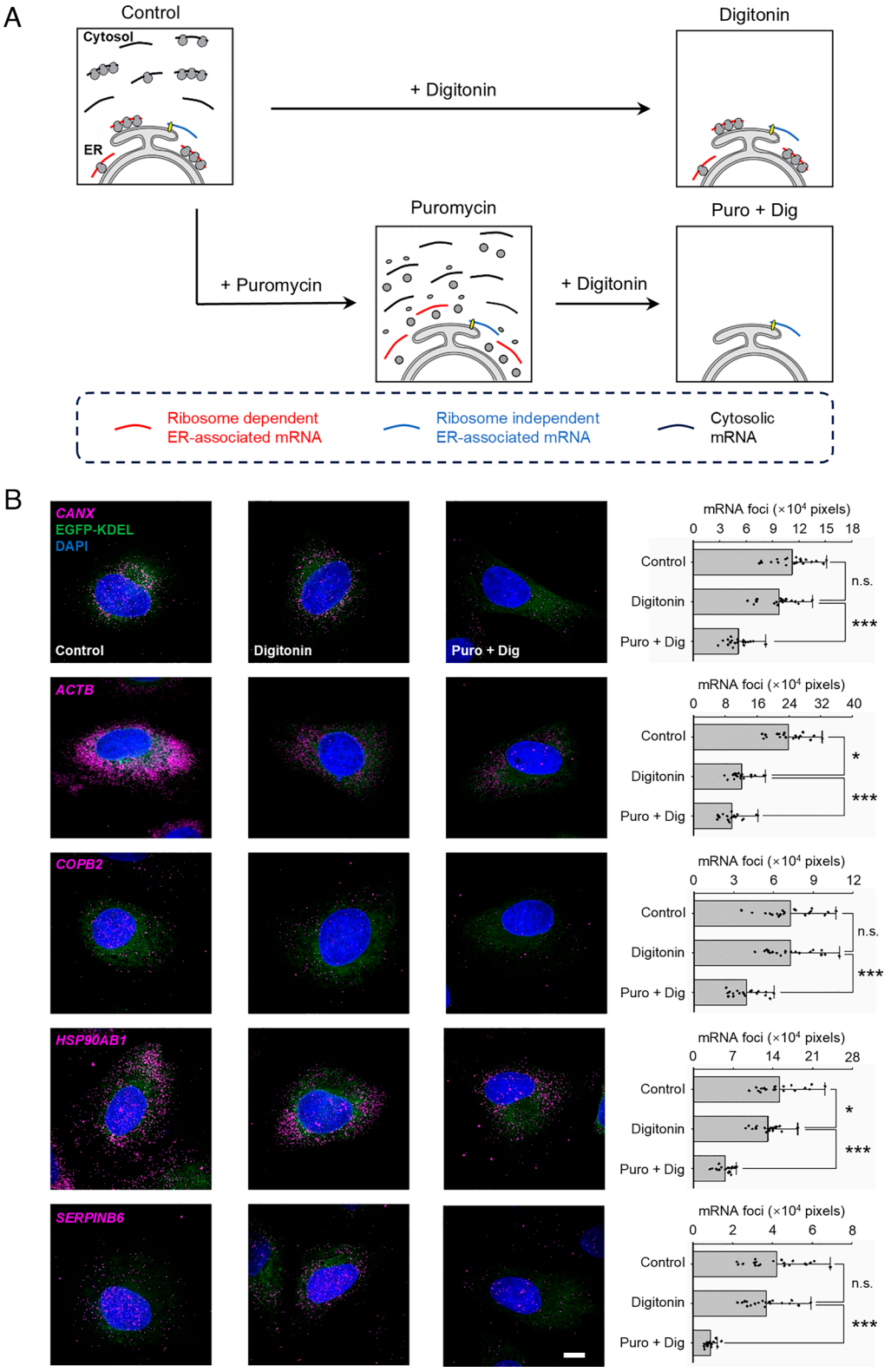

Fig. 3. Single-molecule FISH analysis of local translation at the ER membrane. (*A*) Schematic representation of digitonin extraction (*Top*) and the two-step "Dig + Puro" process (*Bottom*) for detecting local translation at the ERM. Digitonin selectively removes free RNA molecules in the cytosol while retaining ER-bound RNAs. In the "Dig + Puro" strategy, puromycin disassembles ribosomal structures, facilitating the subsequent removal of ER-proximal translation-dependent RNAs by digitonin extraction. (*B*) Representative single-molecule FISH images of *CANX*, *ACTB*, *COPB2*, *HSP90AB1,* and *SERPINB6* mRNAs in HeLa cells. Control: negative control omitting drug treatment. Digitonin: samples subjected to digitonin extraction. Puro + Dig: samples treated with puromycin prior to digitonin extraction. Magenta and green signals represent RNA and ER marker (EGFP-KDEL), respectively. DAPI (blue) stains the nucleus. (Scale bar: 10 μm.) Statistical analysis of smFISH signal is shown on the *Right* (mean ± SD, from 20 cells each). n.s. indicates not significant; * indicates $P < 0.05$; *** indicates $P < 0.001$.

time points but were markedly upregulated by 8 h, with enrichment for ER stress response and protein targeting pathways (*SI Appendix*, Fig. S8*B*). Cluster 5 showed a transient induction at 0.5 h, followed by a sharp decline at 2 h and a secondary increase at 8 h. This cluster was enriched for genes involved in protein metabolism and localization (*SI Appendix*, Fig. S8*C*). Interestingly,

components of the oligosaccharyltransferase (OST) complex (38) were differentially distributed between clusters: *RPN1*, *RPN2*, *STT3A*, *DDOST*, and *MAGT1* were found in cluster 4, while *OST4*, *OSTC*, and *DAD1* were in cluster 5. These patterns indicate dynamic regulation of glycosylation machinery during ER stress, potentially supporting protein folding and cell survival.

To validate translational engagement at the ER membrane under stress, we combined digitonin-based extraction with smFISH imaging. For *HSPA5* (cluster 4), a key UPR gene, we observed robust ERM-localized translation in HeLa cells under both basal and stressed conditions (Fig. 4 *C* and *D*). Similarly, *PRKCSH* (cluster 3), which encodes glucosidase subunit 2β (GLU2B), maintained ERM-associated translation throughout stress exposure (Fig. 4 *E* and *F*). These findings underscore the specificity and utility of optoRibo-seq for capturing dynamic changes in ER-proximal translation during acute stress responses.

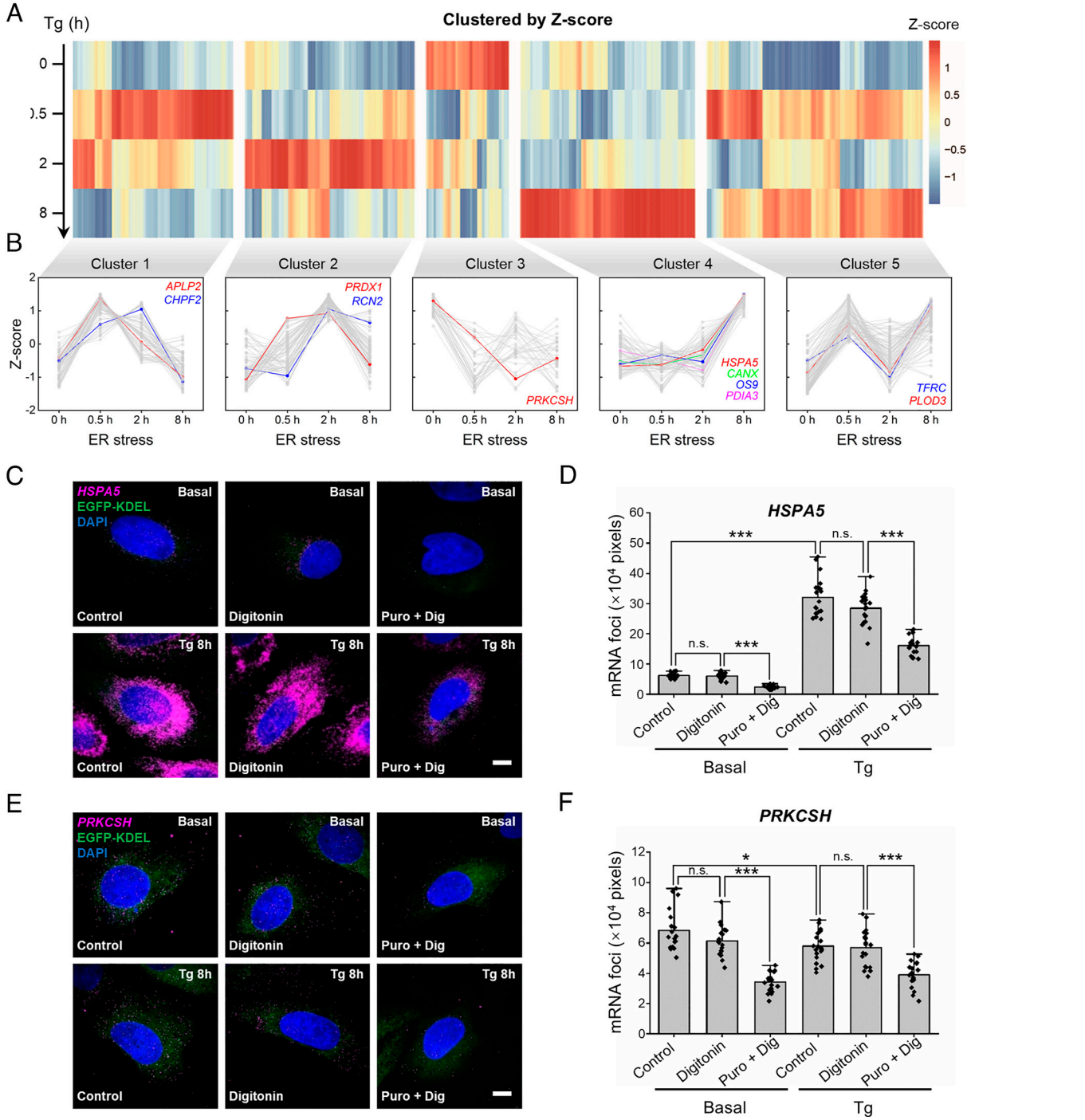

Fig. 4. Dynamic mapping of ER-proximal translatome under stress. (*A*) Heatmap analysis of ER-proximal translatome in HEK293T cells treated with Tg for 0, 0.5, 2, and 8 h. The 331 transcripts identified by optoRibo-seq across the four time points were clustered by Z-score generated from the average FPKM of "ERM Enrich" samples. (*B*) ER-proximal translational dynamics of five clusters of transcripts. (*C–F*) smFISH imaging and analysis of *HSPA5* (*C–D*) and *PRKCSH* (*E–F*) mRNAs under normal and ER stress conditions (Tg 8 h) in HeLa cells. "Control" indicates the negative control without puromycin or digitonin treatment. "Digitonin" refers to samples treated with digitonin extraction, while "Puro + Dig" denotes samples treated with puromycin prior to digitonin extraction. "Basal" represents unstressed cells, and "Tg" represents cells under ER stress induced by Tg. Magenta and green signals represent RNA and ER marker (EGFP-KDEL), respectively. DAPI (blue) highlights nuclear localization. (Scale bar: 10 μm.) Data are presented as mean±SD (n = 20). n.s. indicates no significance; * indicates $P < 0.05$; *** indicates $P < 0.001$.

Multiomic Analysis of Stress-Induced Changes in Transcription and Translation. Under ER stress, the UPR pathway regulates both transcription and translation to restore proteostasis. While global translation is suppressed via eIF2α phosphorylation, UPR-activated transcription promotes the expression of stress-responsive genes. Our ER-proximal translatome profiling revealed dynamic changes in local translation near the ER membrane, particularly increased association of UPR marker transcripts such as *HSPA5*, *PDIA3*, and *OS9* (Fig. 4*B*). To understand how these changes contribute to ER homeostasis, we integrated multiomic analyses to examine transcriptional, translational, and proteomic responses under ER stress (Fig. 5*A*).

The elevated ERM association of transcripts is likely influenced by increased transcriptional output. For example, *HSPA5* mRNA levels rose 4.16-fold following thapsigargin treatment, accompanied by a 2.35-fold increase in ERM-localized translation, as confirmed by smFISH (Fig. 4 *C* and *D* and Dataset S3). This pattern was also observed for slightly downregulated genes such as *PRKCSH*, which showed an 8.1% decrease in mRNA abundance and a 34.0% decrease in ERM-associated translation (Fig. 4 *E* and *F* and Dataset S3). To assess global transcriptional changes, we performed RNA-seq on HEK293T cells under basal and stressed conditions (Fig. 5*A*). DESeq2 analysis identified 534 significantly up-regulated and 362 down-regulated mRNAs (adjusted *P*-value < 0.05; $\log_2$FoldChange > 0.5 or <−0.5) (*SI Appendix*, Fig. S9 *A* and *B* and Dataset S6). Comparing these results with our ER-proximal translatome dataset, we identified 103 transcripts with positively correlated changes in mRNA abundance and ERM translation (*Pearson's r* = 0.60, Fig. 5*B*). Cluster 4 transcripts, including *HSPA5*, *PDIA3,* and *OS9*, showed the strongest correlation (*Pearson's r* = 0.78), indicating that transcriptional upregulation plays a key role in modulating ER-proximal translation during stress. To further disentangle transcriptional and translational contributions, we compared the $\log_2$ fold changes obtained from optoRibo-seq and RNA-seq. This analysis identified five genes with $\Delta\log_2$FC (optoRibo-seq versus mRNA-seq) > 1, including *PMP22*, *SLC38A2*, *EMP3*, *RPL36AL*, and *GMFB*, suggesting stronger regulation at the level of local translation (Fig. 5*B*).

Next, we examined the relationship between ER-proximal and global translational changes at the cellular level. We performed differential expression analysis using the "ERM Input" sample before the optoRibo-seq enrichment process, which is equivalent to directly comparing Ribo-seq data from cells before and after stimulation (Fig. 5*A* and Dataset S6). Among the 331 mRNAs in the dataset, local translational changes in the ERM showed a positive correlation with their corresponding global translational changes (*Pearson's r* = 0.64, Fig. 5*C*). Notably, this correlation was most pronounced for cluster 4 (*Pearson's r* = 0.80), a pattern that aligns well with its previously observed association with transcriptional changes. As the most significantly upregulated transcript in the dataset, *HSPA5* also exhibited the greatest increase in translational level following stimulation. These findings suggest that, for cluster 4 transcripts, elevated transcription levels facilitate both global translation and local translation at the ERM. To further distinguish ER-proximal translation from global translational responses, we compared the $\log_2$ fold changes obtained from optoRibo-seq and global ribosome profiling. This analysis identified twenty genes with $\Delta\log_2$FC (optoRibo-seq versus Ribo-seq) > 1, including *PMP22*, *EMP3*, and *RPL36AL* (Fig. 5*C*). Notably, *SRPRB* and *SPCS1* are involved in ER targeting of translation complexes, while *RNF26* functions as an E3 ubiquitin ligase associated with endocytosis. In contrast, seven genes exhibited $\Delta\log_2$FC < −1, including *SF3B4*, *PSIA4*, *VHL*, *C11orf57*, *PSMC6*, *LZIC*, and *UPF1*, several of which are linked to protein degradation and the ER-associated degradation (ERAD) pathway.

We then examined whether changes in ER-proximal translation correspond to changes in protein levels within the ER lumen. Proteins synthesized at the ER membrane are cotranslationally translocated into the lumen for folding and posttranslational modifications. Using SubMAPP with photoTurbo labeling (20), we profiled the ER lumenal proteome under ER stress (Fig. 5*A*). Among 66 overlapping transcripts, we observed no overall correlation between changes in ERM translation and lumenal protein levels (*Pearson's r* = 0.02). Surprisingly, several UPR-related proteins, including enzymes involved in protein folding (*HSPA5*, *PDIA3, HSP90B1*) and proteins associated with ER glycosylation (*RPN1*, *RPN2*, *STT3A*), showed increased translation but reduced protein abundance in the lumen (Fig. 5*D* and Dataset S6). In contrast, five calcium-binding proteins (*RCN2*, *CALR*, *CANX*, *CALU,* and *CLGN*) displayed a positive correlation, suggesting stress-induced stabilization or reduced degradation of these proteins in response to thapsigargin-mediated disruption of calcium homeostasis. Immunofluorescence analysis revealed a significant increase in the protein levels of BiP (*HSPA5*) and Calnexin (*CANX*) following Tg stimulation (Fig. 5*E*). However, when cells were treated with both Tg and translation inhibitor CHX, this upregulation was markedly attenuated (Fig. 5*E*). Notably, Tg treatment also led to a significant reduction in the colocalization of BiP with ER marker Calnexin (Basal: *Pearson's r* = 0.775; Tg: *Pearson's r* = 0.631), suggesting that the newly synthesized BiP protein is not primarily retained within the ER. In light of the ER lumenal proteomics data, which indicated a substantial decrease in BiP protein within the ER lumen, we speculated that BiP synthesized *via* ER-proximal translation undergoes rapid clearance through distinct pathways, including the ERAD pathway (39) and the active egress (40).

To verify our hypothesis to these observations, we analyzed a previously published prox-SILAC dataset (41) that quantifies protein turnover in subcellular compartments (Fig. 5*A*). Among 38 overlapping ER lumenal proteins, no significant correlation between ERM translation and protein turnover (as measured by metabolic replacement fractions, MRFs) was observed (*Pearson's r* = 0.13, Fig. 5*F* and Dataset S6). However, 28 of 38 proteins exhibited reduced turnover under stress, particularly among calcium-binding proteins (*CANX, CALR,* and *CALU*). Conversely, several ER stress markers (*HSPA5, HSPA13,* and *MESDC2*) showed increased turnover, consistent with both enhanced synthesis and degradation. Given the rapid turnover of BiP in the ER lumen, we treated cells with both Tg to induce ER stress and the proteasome inhibitor MG132 to block the ERAD pathway. Our data showed that MG132 treatment did not significantly alter the cellular abundance of BiP protein (Fig. 5*E*). However, its colocalization coefficient with the ER increased markedly (Tg: *Pearson's r* = 0.631; Tg + MG132: *Pearson's r* = 0.850), indicating that inhibiting ERAD significantly enhances the retention of BiP within the ER (Fig. 5*E*). These findings suggest that elevated turnover rates may account for the discrepancy between increased ER-proximal translation and decreased lumenal protein abundance in some UPR targets. The regulation of other proteins remains complex and likely involves additional layers of posttranslational control.

Discussion

In this study, we developed optoRibo-seq, a strategy for profiling the local translatome of specific subcellular regions in live cells with high spatial and temporal resolution. Leveraging a genetically encoded bioorthogonal decaging system, we engineered a spatially and temporally controlled photoBirA to label nearby ribosomes.

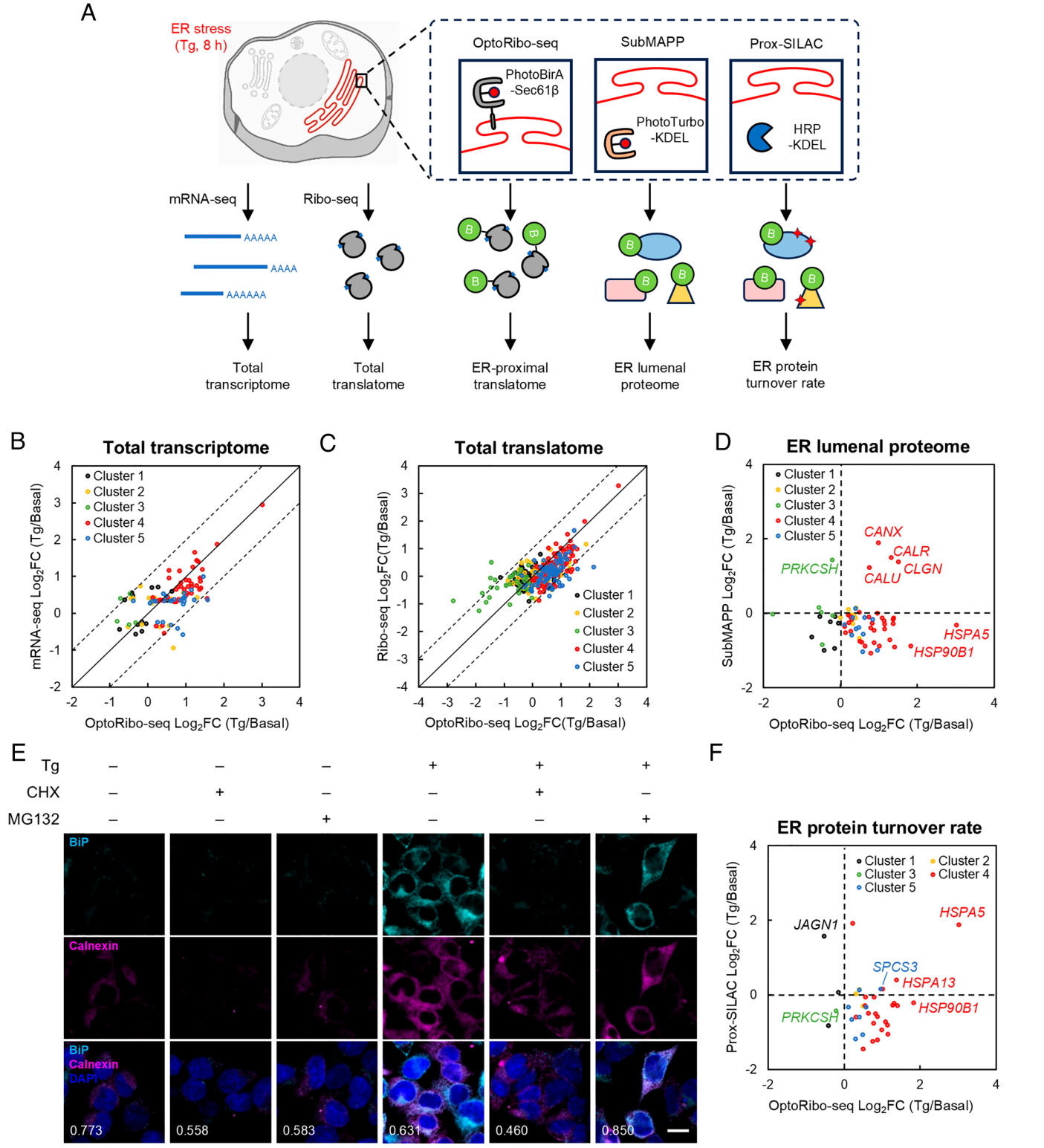

Fig. 5. Multiomics profiling of the ER-associated molecular dynamics under stress. (*A*) Schematic diagram of multiomics profiling of cells under ER stress. HEK293T cells were treated with Tg for 8 h to induce ER stress. (*B* and *C*) Correlation analysis of ER-proximal translatome (optoRibo-seq) with the total transcriptome (*B*) or the total translatome (*C*). Dashed lines indicate the thresholds used to define differences ($\Delta\log_2$FC > 1 or < −1). (*D*) Correlation analysis of ER-proximal translatome with the ER lumenal proteome under ER stress. (*E*) Fluorescent imaging of BiP and Calnexin with or without ER stress (Tg, 8 h), the translation inhibitor CHX (50 μg/mL, 8 h) or the ERAD inhibitor MG132 (2.5 μM, 8 h). Cyan and magenta signals represent BiP and Calnexin localization, respectively. DAPI (blue) highlights nuclear localization. The *Pearson's r* between BiP and Calnexin channels was annotated in the merged channel. (Scale bar: 10 μm.) (*F*) Correlation analysis of ER-proximal translatome with the ER protein turnover rate under ER stress.

This approach bypasses the need for biotin starvation, which was commonly used to reduce background labeling, thus minimizing cellular stress and extending applicability to various subcellular compartments. By reducing the labeling time from 10 min to just 1 min, optoRibo-seq substantially improved spatial precision (Fig. 2 *A* and *B*) and enabled dynamic studies of local translation

in response to stimuli such as ER stress. To improve labeling efficiency, we incorporated S25 as a ribosome tag, which outperformed the commonly used L10a, known for its nonstoichiometric incorporation into polysomes, especially during development (42). Given the growing appreciation of ribosomal heterogeneity across subcellular regions (43), our method provides a valuable alternative for spatially resolved ribosome profiling.

Applying optoRibo-seq to the ERM, we enriched 299 mRNAs, of which 91.0% encoded secretome-associated proteins (Fig. 2 *D* and *E*). Compared with previously reported proximity-specific ribosome profiling data (16), we identified 177 additional ER-proximal transcripts, including 149 annotated secretory mRNAs. These encompassed diverse genes such as *COPB2, HSP90AB1*, *SERPINB6*, and *CLUH*, as well as ribosomal RNA processing factors *RRP1* and *RRP12* (44) and the tRNA-modifying enzyme *QTRT1* (45). Notably, several of these transcripts suggest functional connectivity between the ER and other organelles, including the Golgi apparatus (*COPB2*) and mitochondria (*CLUH*, *G0S2*) (46, 47), underscoring the ER's role in coordinating interorganelle communication.

To explore how ER-proximal translation adapts under ER stress, we applied optoRibo-seq following thapsigargin treatment and identified 311 enriched mRNAs. These were grouped into five clusters based on their translational dynamics (Fig. 4*B*), encompassing numerous UPR markers involved in protein folding, targeting, and ER homeostasis. Unlike transcriptome or proteome analyses alone, ERM-localized translation revealed an intermediate regulatory layer. For instance, *HSPA5* (BiP) showed increased local translation and transcript levels, yet decreased ER protein levels, consistent with enhanced protein turnover (Fig. 5 *B*–*F*). BiP has been previously reported to localize in multiple subcellular compartments and has been shown to translocate from ER to mitochondria (48, 49) or secreted by active egress (40) under ER stress. Our data suggest that in addition to the reported mechanisms, the high level of BiP turnover is also attributable to the ERAD pathways (Fig. 5*E*). In contrast, OST complex components (*RPN1*, *RPN2*, *DDOST*, *STT3A*) exhibited coordinated transcription and translation but reduced protein levels and metabolic flux, whereas calcium-binding proteins (*CANX*, *CALR*, *CALU*) showed increased metabolic rates and elevated protein levels during stress. These results suggest that ER proteostasis selectively preserves key effectors under calcium dysregulation to maintain cell survival.

We attempted to profile the local translatome of OMM using optoRibo-seq, with unsatisfactory results. Local translation at the ER membrane is facilitated by a well-characterized interaction between translating ribosomes and the Sec translocon during cotranslational protein translocation (50). For the optoRibo-seq experiments, ribosomal protein S25 was selected as the bait handle due to its higher cytoplasmic marker signal and lower nuclear background signal. The fact that S25 allowed successful proximal translatome profiling at the ERM but not the OMM suggests suboptimal spatial arrangement between S25 and OMM-targeting photoBirA. Further optimization of the pair of OMM-targeting photoBirA anchor and ribosomal protein handle will be critical for improving labeling efficiency and specificity.

We compared the optoRibo-seq approach with the recently published LOCL-TL method (18). The major advantage of using UV uncaging employed by optoRibo-seq is its low background signal, since photoBirA is completely inactive with its catalytic Lys residue blocked by the UV-active protecting group. Indeed, Western blot analysis of photoBirA after UV illumination for various durations showed excellent temporal control of light-induced activation, whereas a prominent background signal of LOV-BirA was observed in a similar time course analysis (*SI Appendix*, Fig. S10). We also note that the disadvantage of photoBirA is the inability to terminate the labeling reaction promptly. Once activated, the labeling process can only be quenched through removal of ATP from the reaction mixture, such as by desalting of the lysate. In comparison, LOV-BirA has the advantages of being able to be immediately terminated upon turning off blue light. In terms of activation efficiency, photoBirA and LOV-BirA revealed comparable labeling levels upon activation (*SI Appendix*, Fig. S10).

In summary, optoRibo-seq enables high-resolution, minimally perturbative mapping of ribosome-bound mRNAs at specific subcellular locales. Analogous to engineered BirA variants such as BioID (51) and TurboID (52) in proteomic studies, optoRibo-seq provides a versatile platform for dissecting localized translation programs in both membrane-bound and membrane-less organelles across a range of biological contexts.

Methods

Methods related to plasmid construction, western blots, immunofluorescence microscopy, RNA-seq sample preparation, and smFISH are detailed in *SI Appendix*.

Cell Culture and Cell Line Construction. HEK293T and HeLa cells were cultured in DMEM with 10% FBS at 37 °C, 5% CO_2. For lentivirus production, HEK293T cells were transfected at ~60% confluence with pLX304 (1 μg), dR8.91 (1 μg), and pVSV-G (700 ng) using 10 μL PEI. The virus-containing medium was collected 48 h posttransfection, filtered, and 1 mL was used to infect cells at ~70% confluence. After 48 h, medium was replaced with 5 μg/mL blasticidin S for selection. Cells were maintained under 5 μg/mL blasticidin for 7 d with daily medium changes.

Ribosome Labeling, ER Stress Induction, and Cell Harvesting. For optoRibo-seq, S25-AP HEK293T cells were cotransfected with photoBirA plasmids and pEF1-PylRS-(U6-tRNA)×4 using PEI and cultured in 50 μM ONPK containing medium for 18 to 24 h. For ER stress groups, cells were treated with 500 nM thapsigargin at 37 °C for 0.5, 2, or 8 h. Cells were incubated with 50 μM biotin and 100 μg/mL cycloheximide (CHX) for 8 min at 37 °C and then decaged for 1 min by a 365 nm wavelength UV light (43 mW/cm^2) in UV crosslinker (UCP Crosslinker CL-1000, Analytik Jena). For LOCL-TL labeling, S25-AP HEK293T cells were transfected with pcDNA3.1(-)-V5-LOV-BirA-Sec61β, then treated with 50 μM biotin and 100 μg/mL CHX for 8 min at 37 °C and exposed to a 19 mW/cm^2 blue LED for 10 min. All manipulations were done in a biosafety cabinet with internal lights off to avoid premature protein activation.

After labeling, cells were rinsed with ice-cold PBS containing 100 μg/mL CHX for three times, and harvested with polysome buffer (20 mM Tris-HCl pH 7.5, 150 mM NaCl, 5 mM $MgCl_2$, 100 μg/mL CHX, 1 mM DTT) containing 1% Triton X-100, 1× protease inhibitor, 1 U/mL apyrase, and 2 U/mL Turbo DNase into a new 1.5 mL tube.

Monosome Isolation and Enrichment. Lysate was kept on ice for 10 min and cleared by centrifugation at 4 °C and 20,000× g. 2 mL Zeba de-salt spin column was balanced with 1 mL polysome buffer at 4 °C for four times, and the lysate was desalted by the prebalanced column at 4 °C and 1,000× g. Thereafter, the lysate was digested with 3 U/A260 micrococcal nuclease (MNase) and 5 mM $CaCl_2$ at room temperature for 40 min. After digestion, lysis was loaded onto 10 to 50% w/v sucrose gradient in polysome buffer prepared in 14 mL polypropylene tube (Beckman Coulter) by Gradient Master 108 (BioComp), and spun 4 h at 4 °C and 27,500 rpm in an SW-40 rotor (Beckman Coulter). Fractionation was performed on the Piston Gradient Fractionator (BioComp) using EM-1 Econo UV monitor (BioRad) to continually monitor absorbance at 254 nm, and 10% of fractions were isolated as input.

Monosome fractions were concentrated to 1 mL with 100 kDa MWCO ultracentrifugation column, and Triton X-100 was added to a final concentration of 0.01%. Each 100 μL Dynabeads Streptavidin C1 were used for each 15-cm dish of cells. Beads were washed 2× with Buffer A (100 mM NaOH and 50 mM NaCl), 1× with Buffer B (100 mM NaCl), 1× with Buffer C (1× polysome buffer with 0.1% Triton X-100), and coated with Buffer C containing 1 mg/mL BSA and 1 mg/mL yeast tRNA at room temperature for at least 3 h, and then washed 3× with Buffer C. Concentrated fractions were loaded on beads and enriched at 4 °C for 1 h. Enriched beads were washed three times with 1 mL Buffer D (20 mM Tris-HCl pH 7.5, 500 mM NaCl, 5 mM $MgCl_2$, 0.1% Triton X-100, 100 μg/mL CHX, and 1 mM DTT), each for 20 min at 4 °C. After washing, beads were transferred into a

new 1.5 mL tube with 1 mL Buffer C, and digested with 20 U/mL TEV protease in Buffer C with at room temperature for 1 h with vigorous mixing. The supernatant was isolated as enriched samples.

Footprint Isolation and Library Generation. RNAs were extracted from samples by TRIzol reagent and isolated by 15% urea-TBE PAGE. Gel slices containing 20 to 40 nt ribosome footprint were isolated with Ultra low range DNA ladder. Footprints were eluted from gel slice in 300 μL RNA elution buffer (300 mM sodium acetate pH 5.5, 1 mM EDTA, 0.25% SDS, and 1 U/mL SUPERaseIn) by mixing at room temperature and 1,000 rpm overnight, and then re-extracted by TRIzol reagent.

Extracted footprints were suspended with 18 μL nuclease-free water, and dephosphorylated with 1 μL T4 polynucleotide kinase (PNK), 2.2 μLT4 PNK buffer and 1 μL SUPERaseIn at 37 °C for 30 min. After 3′ terminal dephosphorylation, 1 μL ATP (10 mM) was added to phosphorylate the 5′ terminal at 37 °C for 30 min. Phosphorylated footprints were extracted by TRIzol and eluted with 6 μL nuclease-free water for the library generation step. Ribo-seq cDNA libraries were generated by the NEBNext Multiplex Small RNA Library Prep Kit for Illumina. To avoid the generation of dimer, primers were decreased from 2.5 μL to 1.5 μL each sample as MetaRibo-seq technique (53). Generated cDNA libraries were purified by the Monarch DNA purification kit and detected by Fragment Analyzer 12 (AATI).

Quantification and Statistical Analysis. The adaptor sequences of Ribo-seq reads and mRNA-seq reads were removed by Cutadapt (v.1.18), the trimmed Ribo-seq reads that are shorter than 9 were discarded. Reads were quality controlled by FastQC (v0.11.8) to ensure proper library preparation of ribosome footprints. Then the trimmed reads were aligned to an rRNA reference using Bowtie2 (v.2.4.4) to discard the rRNA alignments. The unaligned reads were collected and mapped by hisat2 (v2.1.0) to the human genome assembly GRCh38 (hg38) with gene annotation (v.87) downloaded from Ensembl website. The mapped reads were then counted using htseq-count (v0.7.2). The R package riboWaltz (33) was used for diagnostic analysis and visual inspection of ribosome profiling data.

The subcellular translatome datasets identified by optoRibo-seq were defined by differential expression analysis carried out by R package DESeq2 (v1.34.0). For each DESeq2 analysis, the genes with $\log_2$FoldChange ≥ 0.3 and adjusted P-value < 0.05 were regarded as enriched. The ER-proximal translatome were defined as the overlap between the enriched genes in two DESeq2 analysis: 1) post- versus pre-enrichment of ribosome footprints labeled by photoBirA; 2) postenriched ribosome footprints labeled by ERM localized photoBirA versus ribosome footprints labeled by cytosol localized photoBirA. Three biological replicates were used in each DESeq2 analysis.

Digitonin Extraction. EGFP-KDEL HEK293T or HeLa cells were plated on Matrigel-coated round cell slides in a 24-well plate. At 80 to 90% confluence, cells were rinsed 1× with warm CHO buffer (115 mM potassium acetate, 25 mM HEPES pH 7.4, 2.5 mM $MgCl_2$, 2 mM EGTA, and 150 mM sucrose) and then extracted with CHO buffer containing 0.025% digitonin at 37 °C for 1 min. Puromycin-treated samples were preincubated with 200 μM puromycin for 30 min, with 20 mM EDTA added to extraction buffer for full ribosome disassembly. smFISH procedures are detailed in *SI Appendix*.

Data, Materials, and Software Availability. Data are included in the article and/or supporting information.

ACKNOWLEDGMENTS. This work was supported by the Ministry of Science and Technology (2022YFA1304700, 2018YFA0507600, and 2025YFA0922702), the National Natural Science Foundation of China (32088101), and Beijing National Laboratory for Molecular Sciences (BNLMS-CXXM-202403). P.Z. is sponsored by Bayer Investigator Award. We thank Dr. Wen Zhou at the Analytical Instrumentation Center of Peking University for assistance with mass spectrometry.

Author affiliations: [a]College of Chemistry and Molecular Engineering, Synthetic and Functional Biomolecules Center, Beijing National Laboratory for Molecular Sciences, McGovern Institute for Brain Research, Key Laboratory of Bioorganic Chemistry and Molecular Engineering of Ministry of Education, Peking University, Beijing 100871, China; [b]Academy for Advanced Interdisciplinary Studies, PKU-Tsinghua Center for Life Science, Peking University, Beijing 100871, China; [c]Beijing Advanced Center of RNA Biology, Peking University, Beijing 100871, China; and [d]Chinese Institute for Brain Research, Beijing 102206, China

1. S. Das, M. Vera, V. Gandin, R. H. Singer, E. Tutucci, Intracellular mRNA transport and localized translation. *Nat. Rev. Mol. Cell Biol.* **22**, 483–504 (2021).
2. M. S. Fernandopulle, J. Lippincott-Schwartz, M. E. Ward, RNA transport and local translation in neurodevelopmental and neurodegenerative disease. *Nat. Neurosci.* **24**, 622–632 (2021).
3. V. Rangaraju, S. Tom Dieck, E. M. Schuman, Local translation in neuronal compartments: How local is local? *EMBO Rep.* **18**, 693–711 (2017).
4. M. Gemmer *et al.*, Visualization of translation and protein biogenesis at the ER membrane. *Nature* **614**, 160–167 (2023).
5. C. E. Holt, K. C. Martin, E. M. Schuman, Local translation in neurons: Visualization and function. *Nat. Struct. Mol. Biol.* **26**, 557–566 (2019).
6. C. Li, J. Götz, Somatodendritic accumulation of Tau in Alzheimer's disease is promoted by Fyn-mediated local protein translation. *EMBO J.* **36**, 3120–3138 (2017).
7. D. Piol, T. Robberechts, S. Da Cruz, Lost in local translation: TDP-43 and FUS in axonal/neuromuscular junction maintenance and dysregulation in amyotrophic lateral sclerosis. *Neuron* **111**, 1355–1380 (2023).
8. B. Wu, C. Eliscovich, Y. J. Yoon, R. H. Singer, Translation dynamics of single mRNAs in live cells and neurons. *Science* **352**, 1430–1435 (2016).
9. S. Tom Dieck *et al.*, Direct visualization of newly synthesized target proteins in situ. *Nat. Methods* **12**, 411–414 (2015).
10. H. Zeng *et al.*, Spatially resolved single-cell translatomics at molecular resolution. *Science* **380**, eadd3067 (2023).
11. M. Heiman *et al.*, A translational profiling approach for the molecular characterization of CNS cell types. *Cell* **135**, 738–748 (2008).
12. T. Shigeoka *et al.*, Dynamic axonal translation in developing and mature visual circuits. *Cell* **166**, 181–192 (2016).
13. G. A. Brar, J. S. Weissman, Ribosome profiling reveals the what, when, where and how of protein synthesis. *Nat. Rev. Mol. Cell Biol.* **16**, 651–664 (2015).
14. M. G. Kang, H. W. Rhee, Molecular spatiomics by proximity labeling. *Acc. Chem. Res.* **55**, 1411–1422 (2022).
15. S. Han, J. Li, A. Y. Ting, Proximity labeling: Spatially resolved proteomic mapping for neurobiology. *Curr. Opin. Neurobiol.* **50**, 17–23 (2018).
16. C. H. Jan, C. C. Williams, J. S. Weissman, Principles of ER cotranslational translocation revealed by proximity-specific ribosome profiling. *Science* **346**, 1257521 (2014).
17. C. C. Williams, C. H. Jan, J. S. Weissman, Targeting and plasticity of mitochondrial proteins revealed by proximity-specific ribosome profiling. *Science* **346**, 748–751 (2014).
18. J. Luo *et al.*, Proximity-specific ribosome profiling reveals the logic of localized mitochondrial translation. *Cell* **188**, 5589–5604.e17 (2025).
19. L. M. Sternicki, K. L. Wegener, J. B. Bruning, G. W. Booker, S. W. Polyak, Mechanisms governing precise protein biotinylation. *Trends Biochem. Sci.* **42**, 383–394 (2017).
20. Y. Liu *et al.*, Spatiotemporally resolved subcellular phosphoproteomics. *Proc. Natl. Acad. Sci. U.S.A.* **118**, e2025299118 (2021).
21. Y. Zhu *et al.*, Bioorthogonal cleavage chemistry: Harnessing the bond-break reactions for biomolecule manipulations in living systems. *Chin. J. Chem.* **43**, 553–566 (2024).
22. E. Sanz *et al.*, Cell-type-specific isolation of ribosome-associated mRNA from complex tissues. *Proc. Natl. Acad. Sci. U.S.A.* **106**, 13939–13944 (2009).
23. R. M. Voorhees, R. S. Hegde, Toward a structural understanding of co-translational protein translocation. *Curr. Opin. Cell Biol.* **41**, 91–99 (2016).
24. M. Ashburner *et al.*, Gene ontology: Tool for the unification of biology. *Nat. Genet.* **25**, 25–29 (2000).
25. M. Uhlen *et al.*, Proteomics. Tissue-based map of the human proteome. *Science* **347**, 1260419 (2015).
26. S. Rath *et al.*, MitoCarta3.0: An updated mitochondrial proteome now with sub-organelle localization and pathway annotations. *Nucleic Acids Res.* **49**, D1541–D1547 (2021).
27. S. S. Lam *et al.*, Directed evolution of APEX2 for electron microscopy and proximity labeling. *Nat. Methods* **12**, 51–54 (2015).
28. F. Voigt *et al.*, Single-molecule quantification of translation-dependent association of mRNAs with the endoplasmic reticulum. *Cell Rep.* **21**, 3740–3753 (2017).
29. S. Jagannathan, D. W. Reid, A. H. Cox, C. V. Nicchitta, De novo translation initiation on membrane-bound ribosomes as a mechanism for localization of cytosolic protein mRNAs to the endoplasmic reticulum. *RNA* **20**, 1489–1498 (2014).
30. R. Marom *et al.*, COPB2 loss of function causes a coatopathy with osteoporosis and developmental delay. *Am. J. Hum. Genet.* **108**, 1710–1724 (2021).
31. M. Retzlaff *et al.*, Hsp90 is regulated by a switch point in the C-terminal domain. *EMBO Rep.* **10**, 1147–1153 (2009).
32. M. Jang *et al.*, Dutomycin induces autophagy and apoptosis by targeting the serine protease inhibitor SERPINB6. *ACS Chem. Biol.* **16**, 360–370 (2021).
33. A. E. Darling *et al.*, riboWaltz: Optimization of ribosome P-site positioning in ribosome profiling data. *PLoS Comput. Biol.* **14**, e1006169 (2018).
34. F. M. Fazal *et al.*, Atlas of subcellular RNA localization revealed by APEX-seq. *Cell* **178**, 473–490 (2019).
35. P. Wang *et al.*, Mapping spatial transcriptome with light-activated proximity-dependent RNA labeling. *Nat. Chem. Biol.* **15**, 1110–1119 (2019).
36. C. Hetz, S. Saxena, ER stress and the unfolded protein response in neurodegeneration. *Nat. Rev. Neurol.* **13**, 477–491 (2017).
37. K. Pakos-Zebrucka *et al.*, The integrated stress response. *EMBO Rep.* **17**, 1374–1395 (2016).
38. A. S. Ramírez, J. Kowal, K. P. Locher, Cryo-electron microscopy structures of human oligosaccharyltransferase complexes OST-A and OST-B. *Science* **366**, 1372–1375 (2019).
39. X. Wu, T. A. Rapoport, Mechanistic insights into ER-associated protein degradation. *Curr. Opin. Cell Biol.* **53**, 22–28 (2018).
40. A. S. Lee, Stress-induced translocation of the endoplasmic reticulum chaperone GRP78/BiP and its impact on human disease and therapy. *Proc. Natl. Acad. Sci. U.S.A.* **122**, e2412246122 (2025).
41. F. Yuan, Y. Li, X. Zhou, P. Meng, P. Zou, Spatially resolved mapping of proteome turnover dynamics with subcellular precision. *Nat. Commun.* **14**, 7217 (2023).

42. Z. Shi *et al.*, Heterogeneous ribosomes preferentially translate distinct subpools of mRNAs genome-wide. *Mol. Cell* **67**, 71–83 (2017).
43. D. M. Gay, A. H. Lund, M. D. Jansson, Translational control through ribosome heterogeneity and functional specialization. *Trends Biochem. Sci.* **47**, 66–81 (2022).
44. B. Nieto *et al.*, Identification of distinct maturation steps involved in human 40S ribosomal subunit biosynthesis. *Nat. Commun.* **11**, 156 (2020).
45. C. Fergus *et al.*, The human tRNA-guanine transglycosylase displays promiscuous nucleobase preference but strict tRNA specificity. *Nucleic Acids Res.* **49**, 4877–4890 (2021).
46. J. Gao *et al.*, CLUH regulates mitochondrial biogenesis by binding mRNAs of nuclear-encoded mitochondrial proteins. *J. Cell Biol.* **207**, 213–223 (2014).
47. C. Welch *et al.*, Identification of a protein, G0S2, that lacks Bcl-2 homology domains and interacts with and antagonizes Bcl-2. *Cancer Res.* **69**, 6782–6789 (2009).
48. N. Li, A. Zoubeidi, E. Beraldi, M. E. Gleave, GRP78 regulates clusterin stability, retrotranslocation and mitochondrial localization under ER stress in prostate cancer. *Oncogene* **32**, 1933–1942 (2013).
49. F. C. Sun *et al.*, Localization of GRP78 to mitochondria under the unfolded protein response. *Biochem. J.* **396**, 31–39 (2006).
50. X. Wu, C. Cabanos, T. A. Rapoport, Structure of the post-translational protein translocation machinery of the ER membrane. *Nature* **566**, 136–139 (2019).
51. K. J. Roux, D. I. Kim, M. Raida, B. Burke, A promiscuous biotin ligase fusion protein identifies proximal and interacting proteins in mammalian cells. *J. Cell Biol.* **196**, 801–810 (2012).
52. T. C. Branon *et al.*, Efficient proximity labeling in living cells and organisms with TurboID. *Nat. Biotechnol.* **36**, 880–887 (2018).
53. B. J. Fremin, C. Nicolaou, A. S. Bhatt, Simultaneous ribosome profiling of hundreds of microbes from the human microbiome. *Nat. Protoc.* **16**, 4676–4691 (2021).